NANO MICRO small

Supporting Information

for *Small,* DOI: 10.1002/smll.202002229

Folding at the Microscale: Enabling Multifunctional 3D Origami-Architected Metamaterials

Zhaowen Lin, Larissa S. Novelino, Heming Wei, Nicolas A. Alderete, Glaucio H. Paulino, Horacio D. Espinosa,* and Sridhar Krishnaswamy**

Supporting Information

Folding at the Microscale: Enabling Multifunctional 3D Origami-Architected Metamaterials

Zhaowen Lin, Larissa S. Novelino, Heming Wei, Nicolas A. Alderete, Glaucio H. Paulino, Horacio D. Espinosa*, Sridhar Krishnaswamy**

Mechanical Testing of Origami Metamaterials

In situ SEM compression tests were performed using a commercial Alemnis nanomechanical test platform (Alemnis AG) set up inside an FEI Nova 600 SEM (Figure S1(a)). Both monotonic and oscillatory (Figure S1(b)) displacement profiles were programmed to be exerted by a piezo-driven actuator with a stainless-steel flat punch ($1\ mm$ diameter).

Micropillar Compression Tests

Micropillars were fabricated via two-photon polymerization to assess the constitutive properties of the photocured printing polymer (Figure S2(a)). Figure S2(b) presents the Stress-Strain curves for the micropillar compression experiments described in the Methods Section. Table S1 presents the mechanical parameters derived from each test and overall average values with the corresponding sample standard deviations.

Modeling – Bloch Analysis and Infinite Periodic Structure

Leveraging the periodic nature of the origami-inspired assembly, the mechanical anisotropy and potential tunability of Configuration **A** was explored in terms of mechanical instabilities by employing the Bloch-Floquet formalism in the unfoldable direction (Z-direction). According to the pioneering work of Triantafyllidis and Geymonat et. al, [27, 28] initial periodicity of the structure may break down due to elastic instabilities, giving rise to new periodic patterns within the structure which, depending on their extent, can be classified as

microscopic and macroscopic modes. At the bifurcation point, application of Bloch's Theorem to displacements relates the displacements of nodes in periodic planes (denoted by primed variable) to those of the nodes on the original edges (non-primed variable) by:

$$\boldsymbol{u}(\boldsymbol{X'}) = \boldsymbol{u}(\boldsymbol{X}+\boldsymbol{r}) = \boldsymbol{u}(\boldsymbol{X})e^{j(\boldsymbol{k}\cdot\boldsymbol{r})} = \boldsymbol{u}(\boldsymbol{X})e^{j(k_1 r_1 + k_2 r_2 + k_3 r_3)} \tag{S1}$$

where $\boldsymbol{k}$ denotes the corresponding Bloch wavevector in reciprocal lattice space and $\boldsymbol{r}$ an arbitrary vector of integer components (r_i) in lattice space. The extent of the bifurcation mode (i.e., local to the cell, extending to finite number of cells, and extending to infinite number of cells) is determined by the wavenumbers (k_i) at which the instability condition is satisfied and the magnitude of the lattice vector in a given coordinate direction (Δ_i), viz.:

$$r_i = \frac{1}{k_i \Delta_i} \tag{S2}$$

Bloch analysis was conducted in two steps using the commercial finite element code ABAQUS using the representative volume element (RVE) shown in Figure S4(a) and following well-established procedures.[28-31] While the choice of the RVE is arbitrary, selection of a unit cell with orthogonal lattice vectors (i.e., enclosed by a parallelepiped) was favored on account of the complexity of the boundary conditions dictated by the geometry and the translation operations on which the propagation technique relies.[33] Within the two-step Bloch framework, the first step consisted of subjecting the unit cell to a prestress condition (i.e., displacement in Z-direction) under classical periodic boundary conditions. General classical periodic conditions and equations are shown in Figure S3 and Eqn. S3, respectively.

$$Classical\ Periodic\ BCs.: \begin{cases} \boldsymbol{u}_{x'} - \boldsymbol{u}_x = \boldsymbol{u}_B - \boldsymbol{u}_A & \boldsymbol{\theta}_{x'} - \boldsymbol{\theta}_x = 0 \\ \boldsymbol{u}_{y'} - \boldsymbol{u}_y = \boldsymbol{u}_C - \boldsymbol{u}_A & \boldsymbol{\theta}_{y'} - \boldsymbol{\theta}_y = 0 \\ \boldsymbol{u}_{z'} - \boldsymbol{u}_z = \boldsymbol{u}_D - \boldsymbol{u}_A & \boldsymbol{\theta}_{z'} - \boldsymbol{\theta}_z = 0 \end{cases} \tag{S3}$$

Where pairs $\{(\boldsymbol{u}_{x'};\boldsymbol{u}_x),(\boldsymbol{u}_{y'};\boldsymbol{u}_y),(\boldsymbol{u}_{z'}-\boldsymbol{u}_z)\}$ and $(\boldsymbol{\theta}_{x'};\boldsymbol{\theta}_x),(\boldsymbol{\theta}_{y'};\boldsymbol{\theta}_y),(\boldsymbol{\theta}_{z'}-\boldsymbol{\theta}_z)\}$ denote displacements and rotations, along coordinate directions, of nodes on periodic edges (blue

lines Fig. S3). General displacement loading of the periodic unit cell is achieved by enforcing displacements on reference nodes (Nodes A, B, C and D), located in the corners of the unit cell. Subsequently, a linear perturbation modal analysis step was conducted to extract the natural frequencies of the preloaded structure using Bloch-Floquet periodic boundary conditions, viz.:

$$\boldsymbol{u}_{x'} = \boldsymbol{u}_x\, e^{j(k_x \Delta x)} \quad \boldsymbol{u}_{y'} = \boldsymbol{u}_y\, e^{j(k_y \Delta y)} \quad \boldsymbol{u}_{z'} = \boldsymbol{u}_z\, e^{j(k_z \Delta z)}$$

$$\boldsymbol{u}_{B'} = \boldsymbol{u}_A\, e^{j(k_x \Delta x + k_y \Delta y)} \quad \boldsymbol{u}_{D'} = \boldsymbol{u}_A\, e^{j(k_y \Delta y + k_z \Delta z)} \tag{S4}$$

where pairs $\{\boldsymbol{u}_{x'}; \boldsymbol{u}_x\}, \{\boldsymbol{u}_{y'}; \boldsymbol{u}_y\}, \{\boldsymbol{u}_{z'}; \boldsymbol{u}_z\}$ denote the displacements of nodes in bounding planes of the enclosing parallelepiped and $\boldsymbol{u}_A$, $\boldsymbol{u}_{B'}\boldsymbol{u}_{D'}$ the displacements of specific corner nodes (Figure S4(a)). Both classical and Bloch periodic conditions were implemented via Multi-Point-Constraint (MPCs) Equations in ABAQUS. A single node was constrained during the pre-compression step and eigenvalue extraction at the null wave vector to avoid singularity issues. The procedure was repeated in iterative fashion sweeping over a wide range of wavenumbers (i.e., within the first Brillouin Zone) and prescribed finite deformations in the Z-direction, to determine the minimum strain (i.e., critical strain) at which the system first becomes unstable. Instability is assessed by the change in sign of the system's eigenvalues. Consideration of the three-dimensional periodicity of the RVE, which implies that every combination of wavenumbers (k_1, k_2, k_3) within the interval $[0, 2\pi/\Delta_i]$ must be considered, proved to be a considerable number of computations (e.g., considering five wavenumbers in the $[0, 2\pi]$ interval, it involves 125 simulations for each level of pre-strain).

All Bloch simulations were conducted employing first order quadrilateral and triangular shell elements (ABAQUS element types S4R and S3) with five integration points through the thickness. Following mesh convergence studies, the average element size was established at $0.5\ \mu m$. The IP-DIP photopolymerized polymer post-cure was modeled as linear elastic

(Table S1) with Elastic Modulus derived from average results from micropillar compression tests (SI: *Micropillar compression tests*) and reference values for Poisson's ratio ($\nu = 0.49$) and density ($\rho = 1000\ kg/m^3$), as found in the work by Meza, et al.[3] and Lemma et al.[32] It is noteworthy that mechanical properties of photoresist polymers, especially Young's Modulus, are strongly influenced by manufacturing parameters (e.g., laser power). [32]

Figures S4(c-d) present the eigenvalue-strain curves obtained via implementation of the Bloch framework with finite elements, considering two different sets of wavenumbers. The set corresponding to Figure S4(c) considers five linearly spaced wavenumbers in the range $[0; \pi]$, whereas the set corresponding to Figure S4(d) considers five linearly spaced wavenumbers in the range $[0; \pi/64]$.The latter shows the convergent trend in combinations of wavenumbers approaching the null wavevector, as shown in Figure S4(b), indicating the presence of a long wavelength mode.

While the aforementioned methodology, consisting of a single cell RVE, detects the onset and extent of the geometric instability, it cannot inform on the structural response of the infinite periodic system. To fully capture the behavior of such system, elastic nonlinear geometric finite element analyses of RVEs comprised of multiple stacked unit cells with periodic boundary conditions were conducted. These analyses, performed in perfect and imperfect geometries trace the structural path of the infinite periodic structure. Geometric imperfections in the form of the first buckling mode, global in nature, were added to the perfect geometry to gain insight on the structure's sensitivity to imperfections. The magnitude of the imperfections are normalized by the nominal panel thickness (δ_G/t). Figure S5 presents the stress-strain curves for the aforementioned augmented RVE models, the convergence of the perfect structures to the critical strain predicted by Bloch analysis, and the structural response of the imperfect system with the maximum number of cells analyzed.

Modeling – Imperfection Analysis

Given the extreme sensitivity to geometric imperfections of the mechanical response of thin-walled structures, the structural response of the origami-architected metamaterial in the Z-Direction was studied under global and local geometric imperfections, as well as load imperfections.

First, characterization of buckling modes was carried out, using a linearized buckling analysis consisting of the solution of an eigenvalue problem, to determine the many bifurcation loads of the system. Though such analysis generally overestimate critical loads, the analysis offers insight into the possible mode shapes, which can later be introduced, upon scaling, as imperfections in a subsequent geometric nonlinear analysis. Eigenvalue results of the linear buckling analysis were obtained using Abaqus (* STEP, BUCKLE). The result of the analysis is shown in Figure S6a, including up to the first 40 buckling modes. Selected mode shapes, both local (L) and global (G), (1-3, 25, 33) are shown in Figure S6b.

The response of the structure to a linear combination of local and global imperfections was assessed by superimposing and scaling selected eigenmodes, used as perturbations to the perfect structure. The magnitude of the imperfections are normalized by the nominal panel thickness, δ_L/t for the local imperfection and δ_G/t for the global imperfection. The magnitude of imperfections is selected in agreement with the tolerances observed in experiments ($\frac{\delta_G}{t} = 1, \frac{\delta_L}{t} = 0.5$) and in the form of modes 1,7 (edge affecting modes), 33 (internal affecting modes) and 25, a bowing mode. The elasto-plastic response of the structure with a combination of local and global geometric imperfections is shown in Figure S6c. Additionally, after careful consideration of the experimental setup, the response of the structure under an imperfection in the load application was also considered. Evidenced from the toe region in the force-displacement readings, a small tilt was identified in the loading punch of approximately $\theta_{tilt} \sim 0.8°$. This effect was incorporated in the finite element

simulations by loading the structure with a flat rigid surface with normal and tangential contact conditions including friction. The overall effect of the local and global geometric imperfections together with the aforementioned loading imperfection are depicted Figure S6. The effect of the coefficient of friction in the application of the displacements is shown in Figure S7. In the absence of tangential friction, lateral sliding occurs, causing a deviation from the initial loading path of the structural response. This is followed by convergence problems in the numerical solver (termination indicated by a red cross in Figure S7b). Addition of tangential friction quickly stabilizes the system, allowing it to follow a more complex path in very good agreement with the experimental measurement.

Stiffness Response – Data

Figures 3 and 4 in the main text presents the stress-strain response of Configuration **A** type structures subjected to the oscillatory loading scheme introduced in Figure S1(b). As the amount of compression increases, it can be seen that local folding occurs which then cascades to multiple rows (Figure S8(a-f)) . The stiffnesses reported are the tangent stiffnesses obtained during the oscillatory loading steps at various compression levels. Note that upon unloading, there is a residual compression which subsequently recovers significantly but not completely as discussed in the main text.

For second compression tests following incomplete recovery, the compression data are calculated to include the residual compression to get the percent compression as follows: (deformation imposed by the punch + unrecovered deformation) / original dimension of the as-printed structure.

Figure S9 shows that the response is repeatable for first and second compression of the same sample. Note also that fabrication variances (laser power, writing speed) can change the intrinsic material properties of the polymer, and this can give rise to variations of stiffnesses for the same geometry (the red and black curves in Figure S9) fabricated under different

process parameters. However, the tunability with compression (foldability) follows the same trends. This underscores the need for fabrication processing parameters consistent.

Auxetic Response – Data

The single degree-of-freedom kinematic model for the zipper/aligned assembly (Equation (1)) indicates a geometric instability at the folding angle $= 45^o$, where w_y reaches its maximum (Figure S10). Associated with this is a switch in the sign of the Poisson's ratio (Equation (2) and Figure 3(b,c)). Motivated by this, the chosen configurations **A** and **B** were 3D printed with initial configurations on either side of the instability point. The reversible auxetic behavior of Configuration **B** metamaterials is discussed in the main text. To quantify the ability of Configuration **A** structures to expand/contract in lateral directions in response to axial deformation, the Poisson's ratio was calculated. The change in length was measured by comparative image analysis at two compression stages: zero compression and maximum compression. In this case, the Poisson's ratio should be interpreted as an average instead of an instantaneous value. Owing to the non-uniform deformation of the structures, a consequence of both the folding sequence heterogeneity and end effects, only a region in the middle of the structures was employed for the calculation of Poisson's ratio, as highlighted in Figures S8(b,c,e,f). A summary of the measured Poisson's ratios is presented in Table S2. The Poisson's ratio of the zipper/aligned origami assemblage for Configuration **A** is clearly anisotropic. As listed in Table S2, the (X;Z) structure exhibits a negative Poisson's ratio of $v_{xy} = -0.55$. Note also that the (X;Y) structure presents negligible Poisson effect, $v_{xz} = 0.04$, close to the theoretical value of zero. Since the initial folding angle of Configuration **A** metamaterials was $\psi_0 = 55^o$, these structures always exhibited negative Poisson's ratio v_{xy} with compression, unlike Configuration **B** metamaterials which can exhibit a reversible switch in sign.

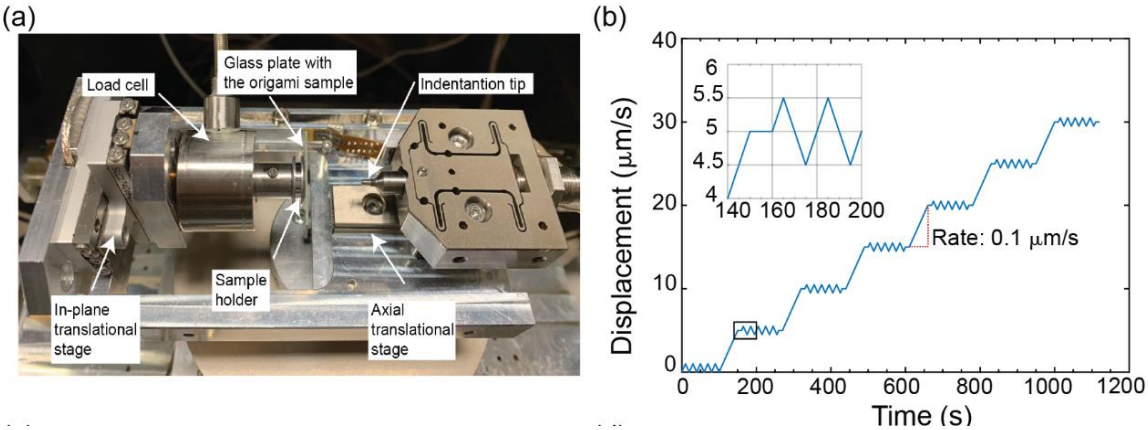

Figure S1: *In situ* SEM Compression Tests. (a) Nanomechanical testing platform. (b) Oscillatory loading profile.

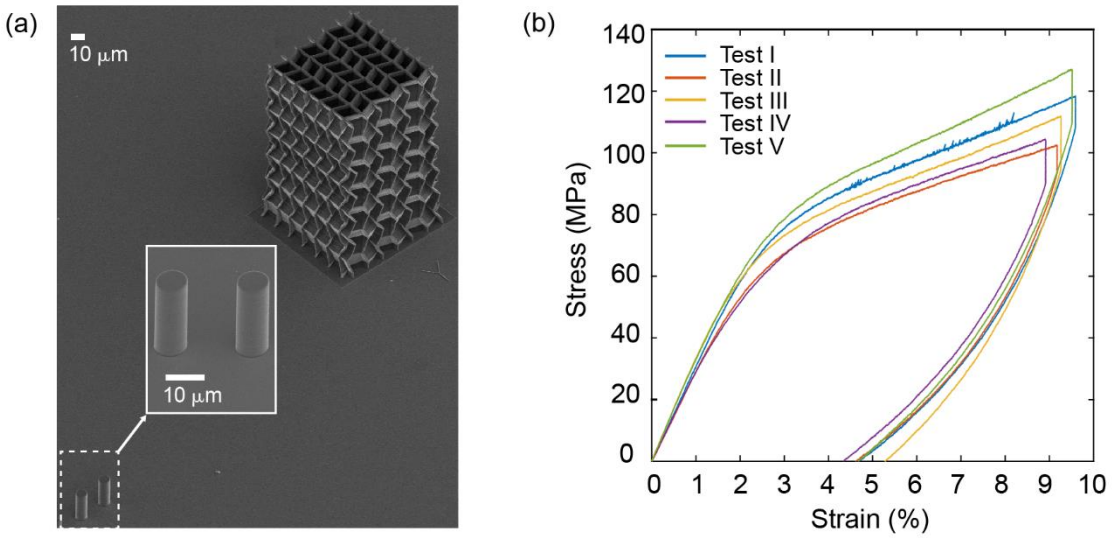

Figure S2. (a) Two-photon lithography printed IP-DIP (Nanoscribe, GmbH) micropillars for material mechanical characterization. (b) Stress-Strain curves from uniaxial compression tests.

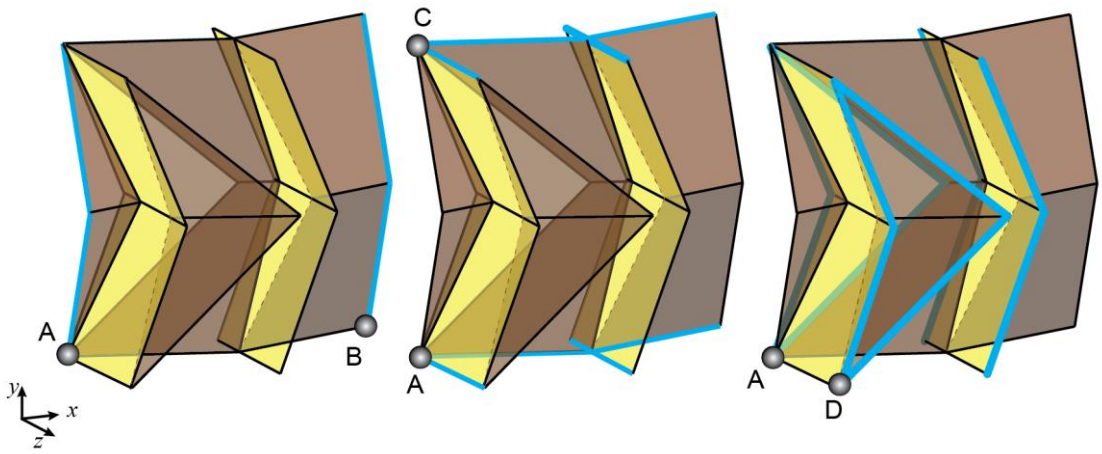

Figure S3. Unit cell considered for the origami metamaterial and reference nodes for implementation of periodic boundary conditions. Periodic edges are highlighted in blue lines.

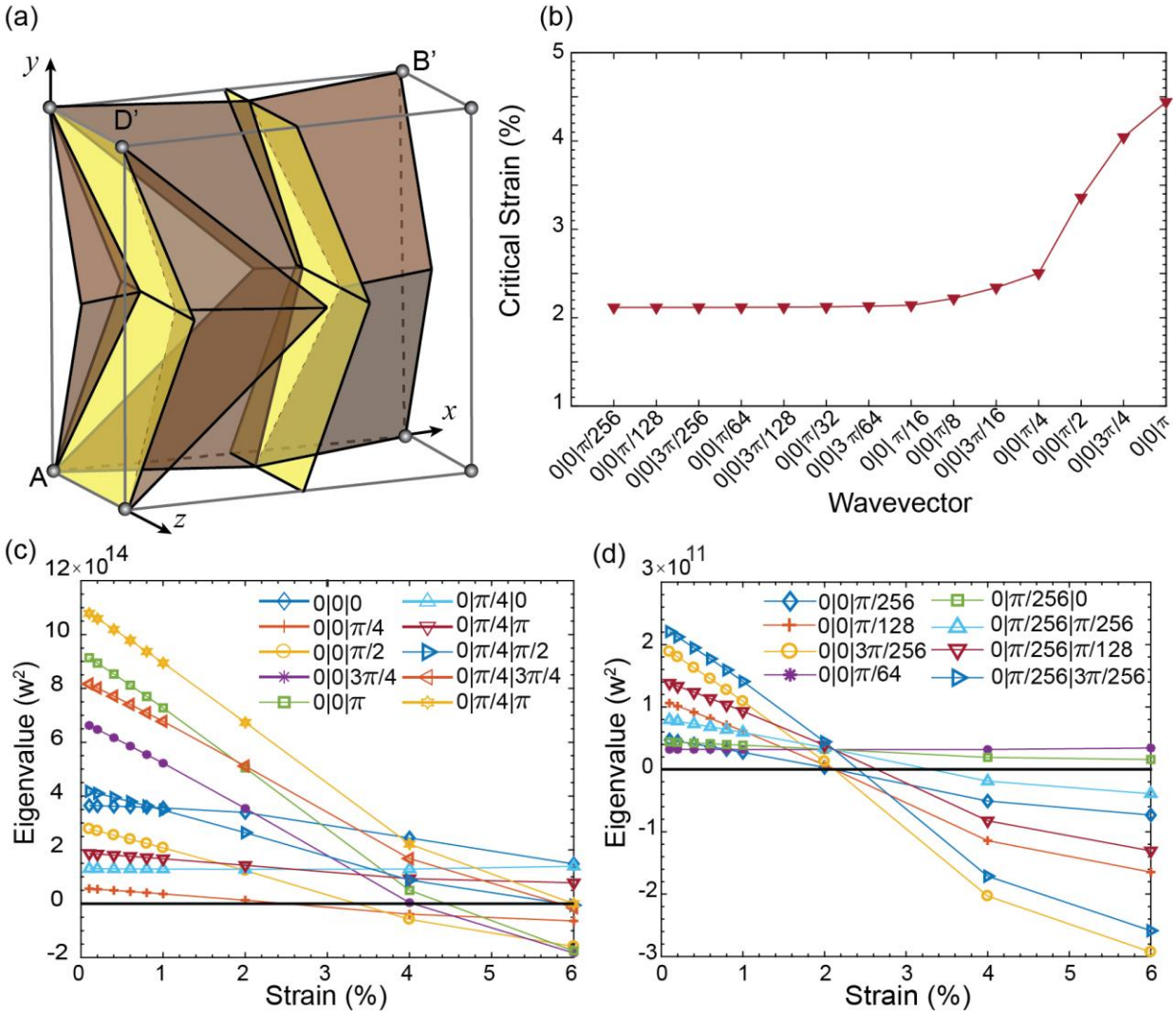

Figure S4. Bloch Analysis of infinite origami assembly. (a) Representative volume element considered for Bloch Analysis with lattice vectors and relevant points. (b) Convergence of critical strain in the neighborhood of the null wavevector. (c) Eigenvalue-Strain curves for wavenumbers in the range [0;π]; (d) Eigenvalue-Strain curves for wavenumbers in the range [0;π/64].

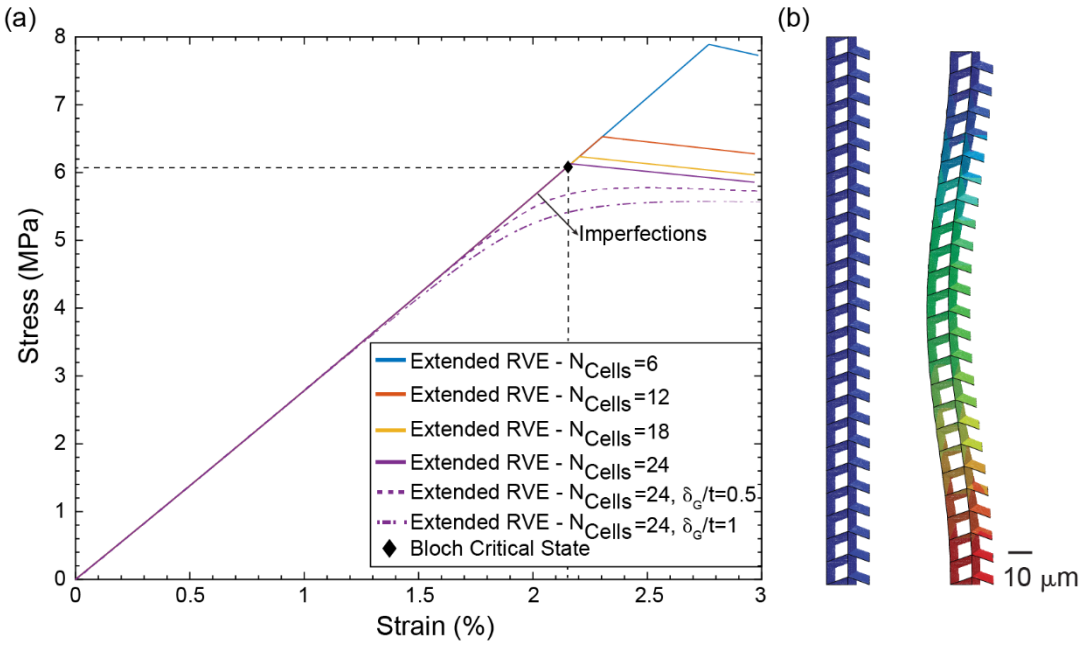

Figure S5. (a) Structural response of perfect and imperfect RVEs with increasing number of unit cells to assess convergence towards the long-wavelength critical strain predicted by the Bloch method. (b) Shape of the long wavelength modes for an RVE with 24 vertically stacked unit cells.

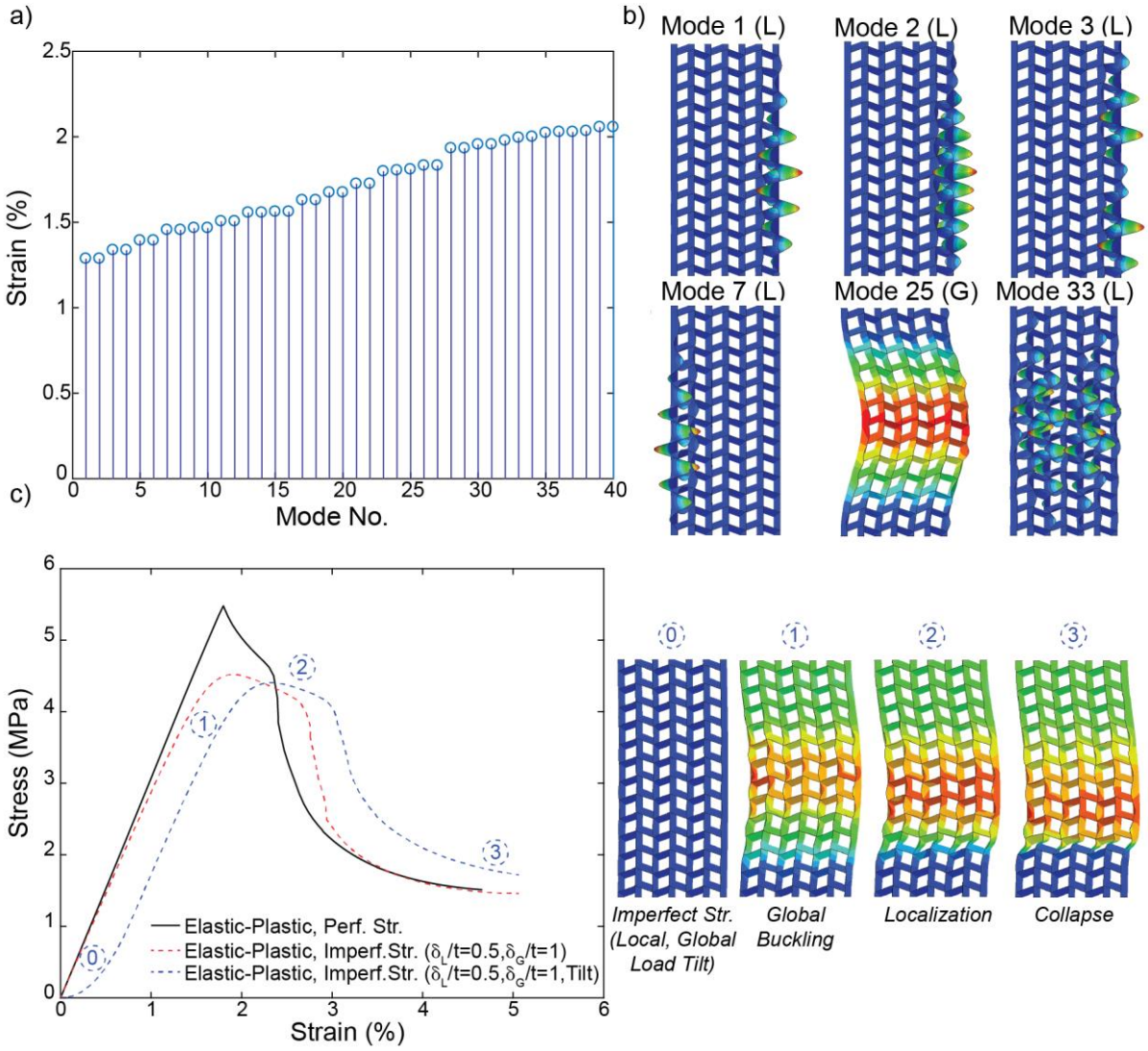

Figure S6. Imperfection analysis for Configuration A, Z-Direction origami-architected metamaterial. (a) Linear buckling analysis, first 40 eigenvalues. (b) Selected local (L) and global (G) modeshapes from linear buckling analysis used as geometric imperfections in subsequent nonlinear finite element analyses. (c) Effect of local, global geometric and load imperfections in the elastic-plastic structural response of the origami structures.

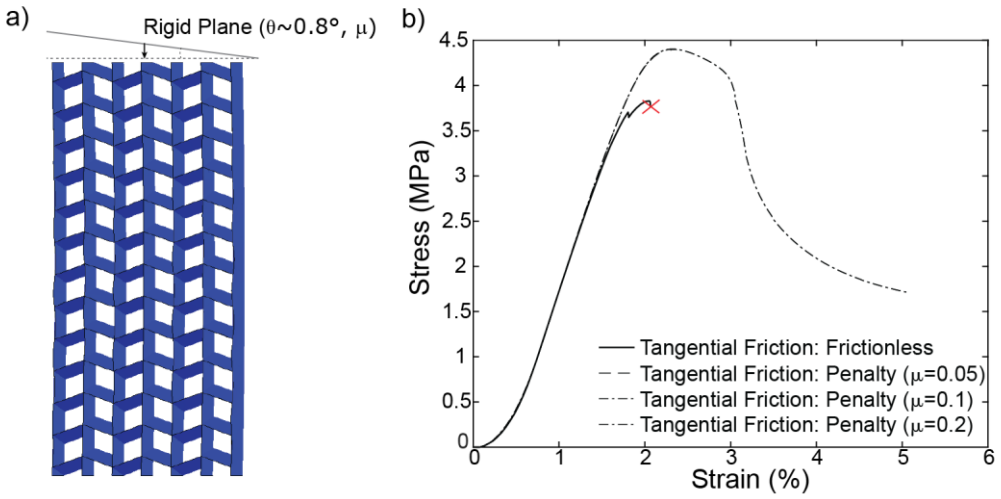

Figure S7. Numerical models with friction. a) Overview of model from Configuration A actuated by means of a rigid, tilted plane. b) Comparison of structural response of Configuration A with tangential friction procedures with varying friction coeficients.

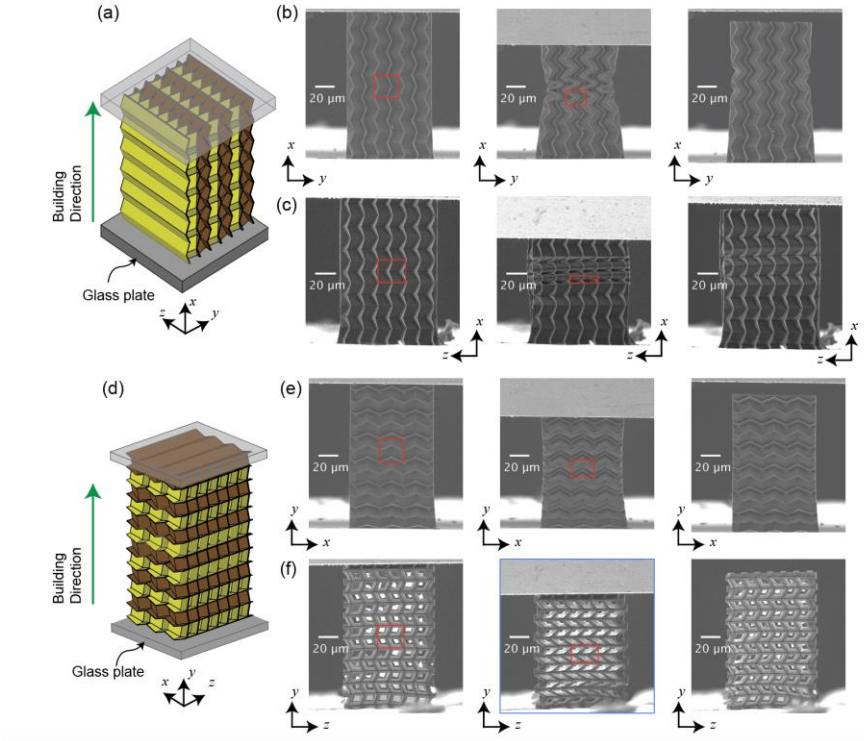

Figure S8. Compression of Configuration **A** metamaterial. (a) Schematic and (b,c) SEM images of the structures compressed along the X-direction and (b) observed from the Z-direction $(X;Z)_1$ at 0% compression (left), at an average 23% compression (center), and after 30 min of relaxation (right); and (c) observed from the Y-direction $(X;Y)_1$ at 0% compression (left), at an average 32% compression (center), and after 30 min of relaxation. (d) Schematic and (e, f) SEM images of the structures compressed along the Y-direction and (e) observed from the Z-direction $(Y;Z)_1$ at 0% compression (left), at an average 23% compression (center), and after 25 min of relaxation (right); and (f) observed from the X-direction $(Y;X)_1$ at 0% compression (left), at an average 32% compression (center), and after 25 min of relaxation (right). Red squares represent regions where the Poisson's ratios were measured.

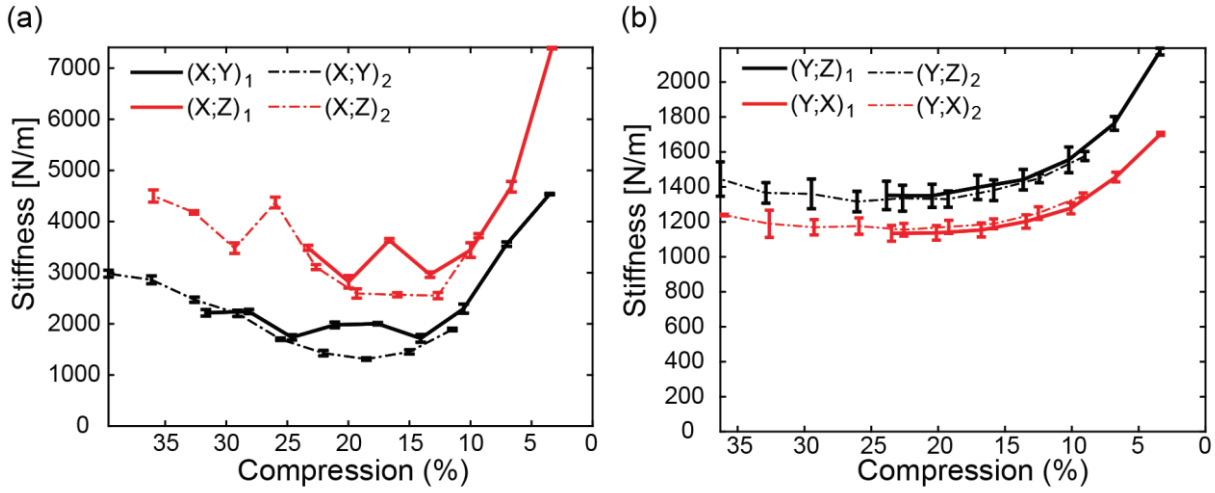

Figure S9. Tunable stiffness relationships for non-monotonic loading of Configuration **A** samples. (a) $(X;Y)_{1,2}$ and $(X;Z)_{1,2}$ samples and (b) $(Y;X)_{1,2}$ and $(Y;Z)_{1,2}$ samples. Note that while $(X,*)_{1,2}$ are the same sample upon first and second compression, $(X,Y)_*$, $(X,Z)_*$, $(Y,X)_*$ and $(Y,Z)_*$ refer to tests on different samples.

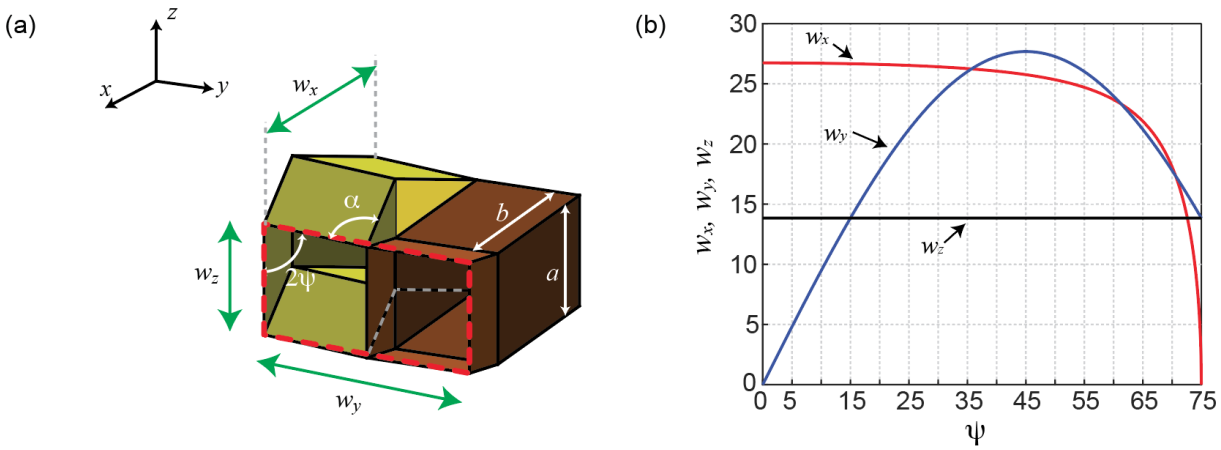

Figure S10: Kinematic model. (a) Unit cell of the zipper-coupled tubes. (b) Plot showing unit cell dimensions as functions of the folding angle ψ for the panel parameters: a=b=13.83μm, panel angle α=75°.

Table S1. Material properties of IP-DIP from micropillar uniaxial compression tests

Test	Young's Modulus (E) (MPa)	Yield Stress (σ_y) (MPa)	Yield Strain (ε_y)	Tangent Modulus (E_p) (MPa)
Test I	3030.83	65.76	0.024	564.67
Test II	2910.20	53.84	0.021	465.83
Test III	3364.74	56.19	0.019	572.16
Test IV	2860.14	51.50	0.020	502.20
Test V	3319.82	61.50	0.021	680.10
Mean	3097.15	57.76	0.021	557.00
Std. Deviation	232.76	5.81	0.0018	81.79

Table S2. Measured Poisson's ratios for Configuration **A** Metamaterials

Compression/observation direction	(X;Z)	(X;Y)	(Y;Z)	(Y;X)
Poisson's ratio (ν)	v_{xy} =-0.55	v_{xz} =0.04	v_{yx} =-0.18	v_{yz} =0.10

Supplementary Movies

Supp. Video 1: Monotonic Compression Test of X-Dir Configuration **A** Metamaterial.

https://northwestern.box.com/s/w41kytvgd9oy154i0quppq57hkioxwh7

Supp. Video 2: Monotonic Compression Test of Y-Dir Configuration **A** Metamaterial.
https://northwestern.box.com/s/jhnuxb47iwxa8xyzwqyeliyzmkrp7lks

Supp. Video 3: Monotonic Compression Test of Z-Dir Configuration **A** Metamaterial.

https://northwestern.box.com/s/12foa1y9pjb0hn9qxna7807n61xjpr2v

Supp. Video 4: Oscillatory Compression Test of X-Dir Configuration **A** Metamaterial.

https://northwestern.box.com/s/f1wwq8xou1xzxr9l6kbadiaykslyjmgs

Supp. Video 5: Compression Test of X-Dir Configuration **B** Metamaterial.

https://northwestern.box.com/s/egv45lp2hxla81c4o8t1te1j075bpxl8

Supp. Video 6: FEM Simulated Compression Test of X-Dir Configuration **B** Metamaterial.

https://northwestern.box.com/s/2tstui0jsmpjnuzgkbkw1it3ay19qy8f

Supp. Video 7: FEM Simulated Compression Test of Z-Dir Configuration **A** Metamaterial.

https://northwestern.box.com/s/6prtrbhggszq96ydzaqd02tcbnzmndh8